



Upper ocean shear in the northern South China Sea

Anzhou Cao¹ · Zheng Guo² · Shuya Wang² · Xu Chen² · Xianqing Lv² · Jinbao Song¹

Received: 16 January 2019 / Revised: 5 July 2019 / Accepted: 9 July 2019 / Published online: 22 July 2019
© The Oceanographic Society of Japan and Springer Nature Singapore Pte Ltd. 2019

Abstract

The shear in the upper ocean of the northern South China Sea (SCS) is examined based on current observations from six moorings in 2010–2011. Spectral analysis results indicate that the sub-inertial currents, near-inertial waves (NIWs), diurnal and semidiurnal internal tides (ITs) dominate the current and shear in the northern SCS. Through comparing current variance and shear caused by these motions, this study shows the great contribution of NIWs to shear: Although NIWs only account for 2–7% of the total current variance, the shear caused by NIWs is approximate one fifth to one-quarter of the total shear. Moreover, the NIWs are dominated by the component with upgoing phase and downgoing energy, whereas the upgoing and downgoing components are comparable in both diurnal and semidiurnal ITs. Because the incoherent component has a larger contribution to shear than the coherent component, the shear of both diurnal and semidiurnal ITs exhibits significant signals with frequencies larger than the spring-neap cycles of approximate 14 days. The larger contribution to shear and smaller proportion in current variance suggest that the incoherent component of ITs has a larger vertical wavenumber than the coherent component. In addition, a case study shows that the mesoscale eddy pair occurring between 22 October and 2 December 2010 does not significantly enhance the ocean shear at two moorings especially below 150 m depth, although it contributes a lot to the current variance.

Keywords Shear · South China Sea · Near-inertial wave · Internal tide · Incoherent component · Mesoscale eddy

1 Introduction

The South China Sea (SCS) is the largest marginal sea of the western Pacific, which is abundant with multi-scale dynamical processes, such as wind-driven circulations, internal tides (ITs), near-inertial waves (NIWs) and mesoscale eddies (MEs). When barotropic tidal currents flow over the Luzon Strait (LS), ITs are generated and propagate into the SCS (Alford et al. 2011, 2015; Buijsman et al. 2014; and references therein). The special double-ridge topography of the LS, intense barotropic tidal currents and stratification make the SCS one of the most significant generation regions of ITs (e.g. Simmons et al. 2004). Combining observations

from moorings, shipboard stations and autonomous gliders, Alford et al. (2015) showed that the time-averaged westward energy fluxes in the SCS are 40 ± 8 kW/m and exceed any other known IT generation site around the world. Based on satellite altimeter and numerical simulation, both Zhao (2014) and Xu et al. (2016) found that ITs radiated from the LS could propagate over 1000 km in the SCS. Moreover, in situ observations indicate that ITs in the SCS exhibit incoherent features, multi-modal structures, seasonal behaviors and spatial variations (Guo et al. 2012, 2018; Lee et al. 2012; Ma et al. 2013; Xu et al. 2013, 2014; Cao et al. 2015, 2017; Shang et al. 2015; Li et al. 2016).

Because of active typhoons and monsoons, the SCS is also one significant region of NIWs. According to the estimation of Wang et al. (2007), there are on average 10.3 typhoons passing through the SCS per year, resulting in active NIWs. However, due to the differences in typhoon characteristics, distances between typhoon centers and moorings, and local conditions, the observed NIWs induced by different typhoons exhibit different intensities, modal structures and decaying time (Sun et al. 2011; Chen et al. 2013; Guan et al. 2014; Yang and Hou 2014; Yang et al.

✉ Jinbao Song
songjb@zju.edu.cn

¹ Ocean College, Zhejiang University, Zhoushan, China

² Physical Oceanography Laboratory, Qingdao Collaborative Innovation Center of Marine Science and Technology (CIMST), Ocean University of China, Qingdao National Laboratory for Marine Science and Technology, Qingdao, China

2015; Zhang et al. 2016a; Cao et al. 2018). Based on the slab model, Li et al. (2015b) estimated that the total near-inertial energy imported from wind is 4.4 GW in the SCS, which is approximately one-quarter of the M_2 tidal conversion at the LS (e.g. Li et al. 2015a; Xu et al. 2016). Besides typhoons, parametric subharmonic instability is another mechanism to generate intense NIWs at the critical latitudes and equatorward of the critical latitudes (Hibiya et al. 1996, 1998, 2002; Nagasawa et al. 2000, 2005; Hibiya and Nagasawa 2004, Xie et al. 2011) in the SCS.

In addition to ITs and NIWs, MEs are another active dynamic process in the SCS. Based on an 8-year (1993–2000) altimeter dataset, Wang et al. (2003) detected a total of 86 MEs corresponding to 10.8 MEs per year in the SCS. By analyzing more than 7000 MEs and their tracks, Chen et al. (2011) found that MEs in the SCS are mainly generated in a northeast-southwest direction and southwest of the LS. Moreover, MEs in the SCS show notably intra-annual and interannual variations (Chen et al. 2009; Cheng and Qi 2010; Sun et al. 2016) and exhibit a different three-dimensional structure from those reconstructed by combining satellite altimeter data and concurrent Argo profiling float temperature/salinity data in the open ocean (Zhang et al. 2014, 2016b).

Recent studies have summarized the advances and showed the challenges in the parameterization of ocean turbulent mixing (MacKinnon et al. 2017; Fox-Kemper et al. 2019). In the parameterization, ITs, NIWs, mesoscale and submesoscale processes are important dynamics and contribute a lot to ocean turbulent mixing. However, how to accurately parameterize these processes remains a great challenge. According to Alford et al. (2017), shear instability is thought to drive the most turbulence in the ocean, making the characterization of the sources, scales, and variability of ocean shear an important goal of physical oceanography. In the SCS, active ITs, NIWs and MEs can cause shear and hence make contributions to the enhancement of turbulent mixing (Tian et al. 2009; Alford et al. 2011, 2015; Guan et al. 2014; Yang et al. 2017; Cao et al. 2018). Therefore, investigating the shear caused by ITs, NIWs and MEs would deepen our understanding of their contributions to turbulent mixing and contribute to the development of parameterization of turbulent mixing in the SCS. However, due to scant in situ observations, relevant studies are rare. Based on a 2-month moored current time series on the continental shelf of the northwestern SCS, Xu et al. (2011) compared the shear caused by diurnal (D1) and semidiurnal (D2) ITs. Results indicated that the shear caused by D1 ITs was stronger than that caused by D2 ITs around 45 m depth, whereas higher-mode D2 ITs produced larger shear than D1 ITs below 45 m depth, the node depth of mode-1. Xu et al. (2013) further examined the shear induced by ITs and NIWs on the continental slope of the northwestern SCS. Results

showed that the shear caused by NIWs was smaller than that caused by ITs at most times, but was significantly enhanced and exceeded the shear caused by ITs by a factor of 2 to 3 in the upper layer when the typhoon passed by. These studies reveal some features of shear on the continental slope and shelf of the SCS, but the shear in the SCS Basin and near the LS remains unknown. On the other hand, these studies did not focus on the shear caused by MEs. The SCS Internal Wave Experiment (Guan et al. 2014; Cao et al. 2017, 2018) deployed several moorings in the northern SCS in 2010–2011 and provided a chance to better understand the ITs, NIWs and MEs in this area. In this study, we will show the shear induced by these motions in the upper ocean of the northern SCS by analyzing current observations from six moorings.

The paper is organized as follows. The mooring observations and data analysis methodology are introduced in Sect. 2. In Sect. 3, the spatial and temporal features of shear caused by NIWs and ITs are displayed and a case study is performed to evaluate the contribution of MEs to shear. Finally, the paper is completed with a discussion in Sect. 4 and conclusions in Sect. 5.

2 Data and methodology

2.1 Mooring data

In this study, current observations from six moorings (MP1–MP6) of the SCS Internal Wave Experiment are used. Each mooring was equipped with a 75 kHz upward-looking acoustic Doppler current profiler (ADCP) to measure currents in the upper ocean. Positions of these moorings are displayed in Fig. 1a and b shows the observation periods. Note that the observation periods of MP1 and MP2 are from March to August 2010, which are prior to those of other moorings. The observational data are provided by the Physical Oceanography Laboratory, which have a temporal resolution of 1 h and a vertical interval of 5 m. Under the influence of background currents, internal waves and MEs, the moorings occasionally had vertical excursions, resulting in gaps in the current observations. Therefore, linear interpolation is used to fill in the gaps in the temporal domain if raw observations covered more than 95% of the total observation period at the corresponding depth. After linear interpolation, the effective ranges of currents at moorings MP1–MP6 are 85–405 m, 50–535 m, 125–455 m, 80–355 m, 50–420 m and 55–490 m, respectively (Table 1).

During the observation periods of these moorings, active ITs, NIWs and MEs were found. The coherent and incoherent features, seasonal behaviors and spatial variations of D1 and D2 ITs in this area were investigated by Cao et al. (2017). Figure 1a shows tracks (<http://tcdata.typhoon.org>).

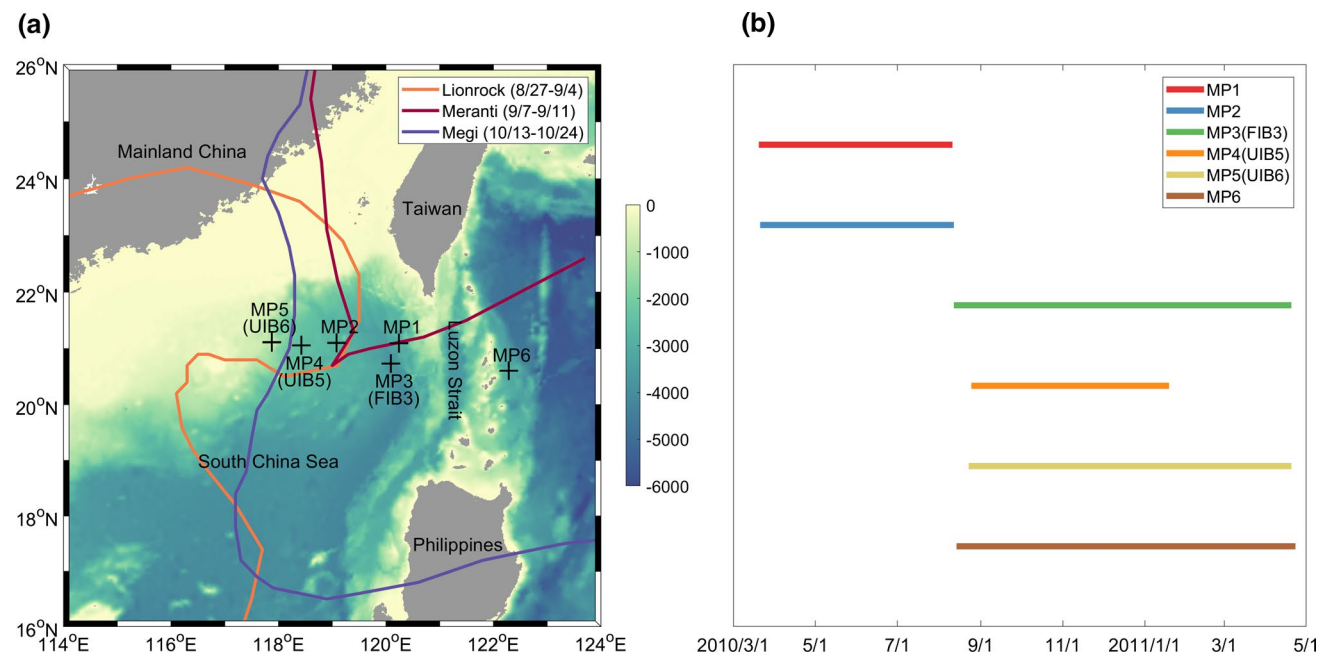


Fig. 1 **a** Bathymetry (shading, unit: m) of the northern SCS, mooring positions (black pluses) and tracks (colorful curves) of typhoons Lionrock, Meranti and Megi in 2010. **b** Observation periods of the

moorings. Note that the observation periods of MP1 and MP2 are prior to the passage of three typhoons

Table 1 Detailed information of moorings MP1-MP6

Mooring	Position	Water depth (m)	Instrument	Instrument depth (m)	Range depth ^a (m)
MP1	120°15'E, 21°05'N	2895	75 kHz ADCP	~650	85–405
MP2	119°05'E, 21°06'N	2719	75 kHz ADCP	~650	50–535
MP3 (FIB3)	120°06'E, 20°44'N	3745	75 kHz ADCP	~515	125–455
MP4 (UIB5)	118°26'E, 21°04'N	2480	75 kHz ADCP	~408	80–355
MP5 (UIB6)	117°53'E, 21°06'N	968	75 kHz ADCP	~442	50–420
MP6	122°17'E, 20°36'N	3116	75 kHz ADCP	~517	55–490

^aRange depth indicates the available depth range of currents after linear interpolation

cn) of typhoons Lionrock, Meranti and Megi in 2010, which caused intense NIWs at MP3, MP4 and MP5 (Cao et al. 2018). In addition to the three NIW events induced by typhoons, two other NIW events were found at MP5 in December 2010 and March 2011. The real mechanisms of the two NIW events remained unknown, but Cao et al. (2018) ruled out the local winds, lateral propagation, and parametric subharmonic instability as causes of these NIWs. Moreover, MP6 captured the NIWs induced by typhoon Chaba in October 2010 in the western Pacific. Figure 2 shows the sea level anomaly and surface geostrophic currents (<http://www.aviso.oceanobs.com>) during 15 October to 10 December 2010, from which a ME pair [a cyclonic eddy (CE) and an anticyclonic eddy (AE)] was detected. Besides this ME pair, MEs were also visible in other months, which are not shown here.

2.2 Methodology

Based on the interpolated currents, the total shear is calculated as follows:

$$s_x = \partial u / \partial z, s_y = \partial v / \partial z, \text{ and } s = \sqrt{s_x^2 + s_y^2} \quad (1)$$

where $u(s_x)$ and $v(s_y)$ are the zonal and meridional components of currents (shear), $\partial u / \partial z$ and $\partial v / \partial z$ are the first-order derivatives of u and v with respect to depth. Based on the two-dimensional Fourier transform, the wavenumber frequency spectra of currents and total shear are calculated to show the temporal and vertical scales of the dominant motions. Then a fourth-order Butterworth filter is employed to extract sub-inertial currents (SICs), NIWs, D1 and D2 ITs. Note that the SICs contain both MEs and low-frequency

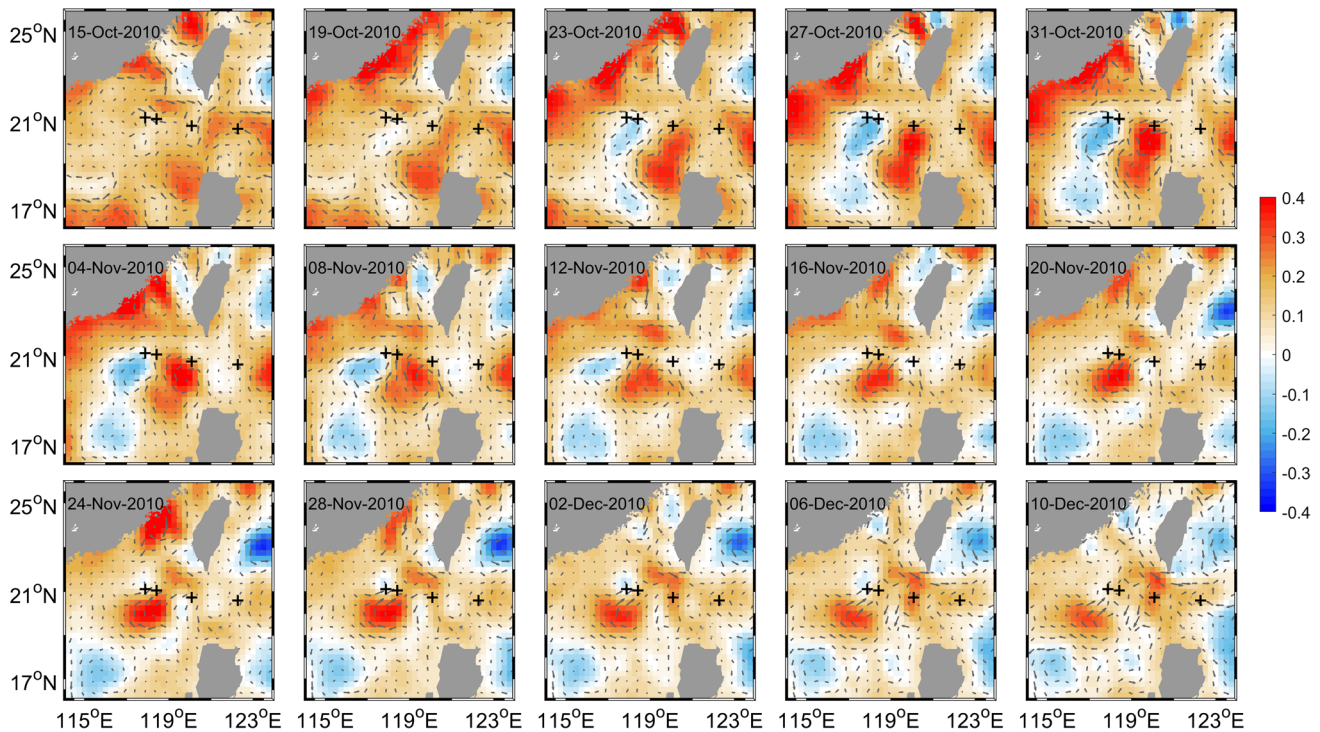


Fig. 2 The sea level anomaly (shading, unit: m) and surface geostrophic currents (gray quivers) from 15 October to 10 December 2010 with an interval of 4 days. The black pluses denote MP3–MP6 of which the observation periods cover 15 October to 10 December 2010

background currents, such as the Kuroshio. According to the spectral analysis results (Fig. 3) and previous studies (Zhang et al. 2013; Guan et al. 2014; Cao et al. 2017), the cutoff frequencies for SICs, NIWs and D1 and D2 ITs are

[0, 0.4] cpd, [0.58, 0.81] cpd, [0.80, 1.20] cpd and [1.73, 2.13] cpd, respectively. Because the six moorings nearly located at the same latitude, the same cutoff frequencies are used for MP1–MP6. The local inertial frequency (f) at the

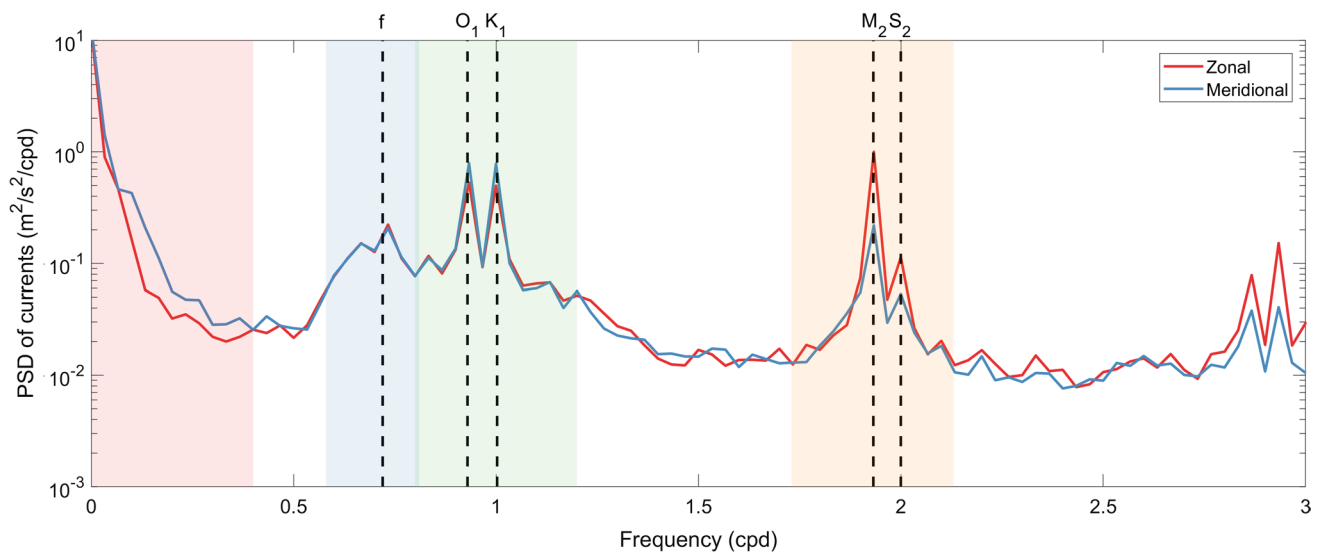


Fig. 3 Depth-averaged power spectral densities (PSDs) of the zonal (red) and meridional (blue) currents at MP4. The whole observation is divided into eight one-month time series with 50% overlapping so that the spectra have a freedom of 16 and a frequency bandwidth of

0.033 cpd. The vertical dashed lines indicate the local inertial frequency f and dominant tidal frequencies O_1 , K_1 , M_2 and S_2 . The light red, blue, green and orange shadings denote cutoff frequencies for SICs, NIWs, D1 and D2 ITs, respectively (color figure online)

six moorings is about 0.72 cpd (corresponding to a period of 33.3 h), therefore, the near-inertial band is about $[0.80, 1.13]f$. As shown in Fig. 3, the four frequency bands are wide enough to extract the SICs, NIWs, D1 and D2 ITs. Moreover, the filter is run twice (forward and backward) over current time series when extracting SICs, NIWs and ITs at each mooring. Based on the bandpass filtered currents, the shear caused by SICs, NIWs, D1 and D2 ITs is calculated according to Eq. (1). At the same time, to evaluate the intensities of SICs, NIWs and ITs, current variance (Xu et al. 2013, 2014) is calculated as follows:

$$\text{Var} = u^2 + v^2. \tag{2}$$

Because the product of current variance and half of the mean density is horizontal kinetic energy, the current variance can reflect the intensity of motions and its variation can be regarded as variation of energy. In addition, we extract upgoing and downgoing components of NIWs and ITs following MacKinnon et al. (2013) to explore their vertical pattern and propagation.

Due to the modulation of varying background conditions and stratification, ITs exhibit intermittency and part of internal tidal energy is transferred to frequencies outside the deterministic tidal frequencies (van Haren 2004; van Aken et al. 2007; Nash et al. 2012; Xu et al. 2014; Liu et al. 2016). In other words, incoherent ITs generate. In this study, the shear caused by coherent and incoherent components of ITs is investigated. The coherent and incoherent components of ITs are calculated following Zhao et al. (2010), Xu et al. (2013) and Pickering et al. (2015):

$$u' = u'_c + u'_i \text{ and } v' = v'_c + v'_i, \tag{3}$$

where u' and v' are the zonal and meridional currents of D1 or D2 ITs which are extracted through bandpass filtering introduced above, and subscripts c and i denote the coherent and incoherent components, respectively. The coherent component of D1 (D2) ITs is the hindcast of the K_1, O_1, P_1 and $Q_1 (M_2, S_2, N_2 \text{ and } K_2)$ tidal currents which are calculated using the T_Tide software package (Pawlowicz et al. 2002). Subtracting the coherent component from the bandpass filtered internal tidal currents, the incoherent component is obtained. Thereafter, the shear caused by the coherent and incoherent components of ITs is calculated according to Eq. (1).

3 Results

3.1 Wavenumber frequency spectra

The vertical wavenumber and frequency characteristics of currents and shear are first examined by means of wavenumber frequency spectra. Figure 4 displays the wavenumber frequency spectra of interpolated currents and total shear at MP5 as an example. In the wavenumber frequency spectra, positive and negative frequencies correspond to counterclockwise (CCW) and clockwise (CW) rotation, respectively, and positive and negative vertical wavenumbers m correspond to upward and downward energy propagation, respectively (Alford et al. 2017). In the current spectra, large spectral densities mainly appear around the frequencies of $0, \pm f, \pm K_1$ and $\pm M_2$, confirming that the motion here is dominated by SICs, NIWs, D1 and D2 ITs. The spectral densities at the $-f, -K_1$ and $-M_2$ frequencies are much

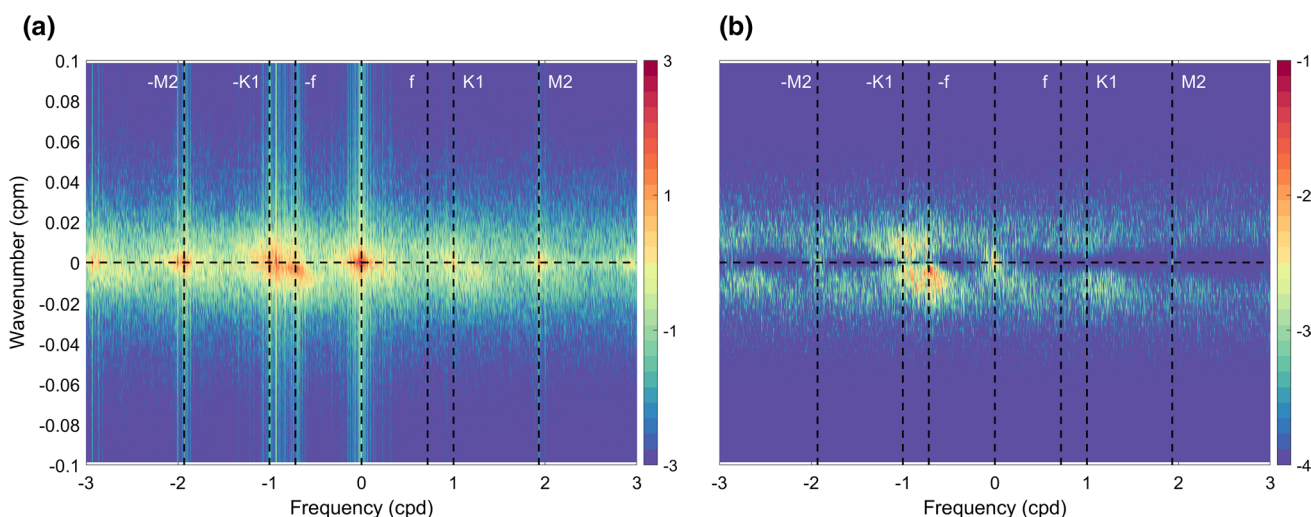


Fig. 4 Wavenumber frequency spectra (shading, unit: $m^2 s^{-2} cpd^{-1} cpm^{-1}$ for current and $s^{-2} cpd^{-1} cpm^{-1}$ for shear) of **a** currents and **b** shear at MP5 in the log form. Vertical dashed lines

indicate frequencies ($0, \pm f, \pm K_1, \pm M_2$) of dominant motions (SICs, NIWs, D1 and D2 ITs) and the horizontal dashed line indicates $m=0$

larger than those at the f , K_1 and M_2 frequencies, suggesting that the internal waves here are dominated by the CW rotating component, which is consistent with the theory of internal waves in the northern hemisphere. For D1 and D2 ITs, the corresponding spectral densities at $m > 0$ and $m < 0$ are comparable, suggesting that both the upward and downward propagation components are important in the ITs. However, the NIWs have a larger spectral density at $m < 0$, suggesting that they are dominated by the component of downward energy (upward phase) propagation, which will be shown in detail in the following section. The shear spectra show a different pattern from the current spectra. As shown in Fig. 4b, the NIWs and D1 ITs dominate the shear spectra, whereas the spectral densities in the frequency bands of SICs and D2 ITs are much smaller. The reason is that the vertical wavenumber of NIWs and D1 ITs is larger than that of D2 ITs and SICs, which is clearly shown in Fig. 4a. Similar results are found at other moorings, which are not shown here.

3.2 Upgoing and downgoing components in NIWs and ITs

In this section, the upgoing and downgoing components of NIWs and ITs are examined. According to Alford et al. (2017), there are two methods to extract the upgoing and downgoing components of internal waves: One is to separate the current/shear into CCW and CW rotating components with depth, which correspond to upgoing and downgoing waves for a linear wave field, respectively (Leaman and Sanford 1975). The other is based on the inverse Fourier

transform of spectral density in the four quadrants of the wavenumber frequency spectra (Fig. 4) to obtain the current/shear components of upward/downward propagation and CW/CCW rotation (MacKinnon et al. 2013). In this study, we adopt the second method. Figure 5 displays the NIWs, D1 and D2 ITs as well as their upgoing and downgoing components at MP5 during 20 October to 4 November 2010 (during the passage of typhoon Megi) and Fig. 6 shows the result for zonal shear. Note that in the inverse Fourier transform, the spectral density at $m = 0$ (corresponding to the vertically averaged current/shear) is not taken into consideration. Therefore, the sum of the upgoing and downgoing components may be smaller than the current/shear of NIWs and ITs. As shown in Fig. 5, the upgoing component of NIWs almost has the same pattern as the NIWs and it is much larger than the downgoing component, suggesting that the NIWs induced by typhoon Megi are dominated by the upgoing component. Because phase and energy of internal waves have opposite propagating directions in the vertical direction, the near-inertial energy induced by Megi mainly propagates downward to the deep ocean. This result is consistent with previous analysis in Cao et al. (2018) and other studies about NIWs in the SCS (e.g. Yang and Hou 2014; Zhang et al. 2016a). Similar results can be found for the NIWs caused by typhoons Lionrock, Meranti and Chaba as well as the moderate winds at most time at the moorings. In contrast to the NIWs, both D1 and D2 ITs have an intense vertically averaged component and comparable upgoing and downgoing components at the six moorings. Due to the limited measuring range (Table 1), the vertically

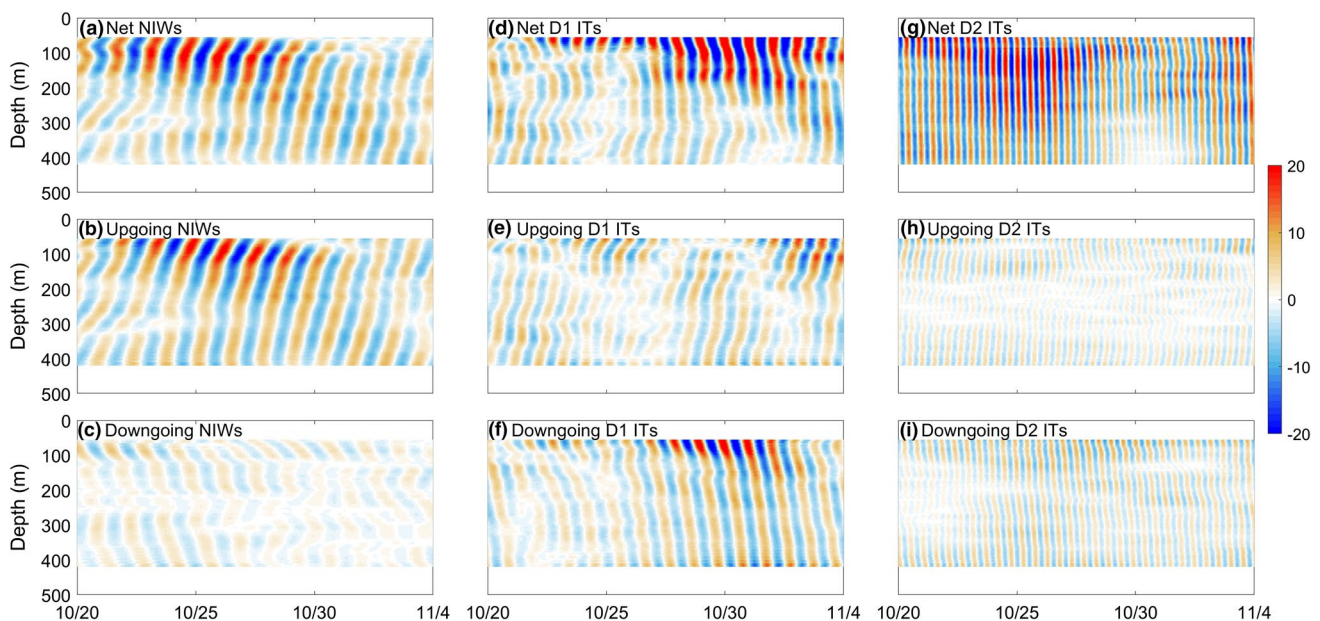


Fig. 5 Zonal currents of **a–c** NIWs, **d–f** D1 and **g–i** D2 ITs as well as their **b, e, h** upgoing and **c, f, i** downgoing components at MP5. Note that the “upgoing” and “downgoing” here denote the propagation of phase, corresponding to downward and upward energy propagation, respectively

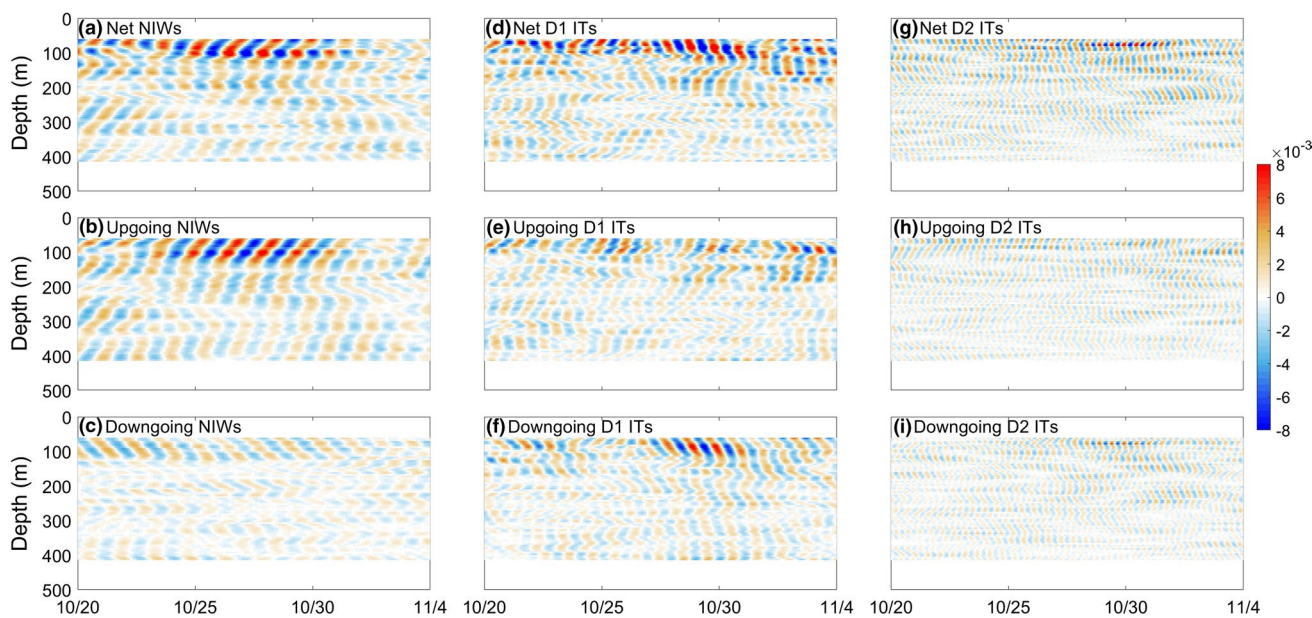


Fig. 6 Same as Fig. 5 but for zonal shear

Table 2 Proportions of the upgoing and downgoing components in current variance and shear of NIWs and ITs at the six moorings (Subscripts “up” and “down” denote the upgoing and downgoing components, respectively)

Mooring	Motion	Current variance		Shear	
		Var _{up} /Var (%)	Var _{down} /Var (%)	s _{up} /s (%)	s _{down} /s (%)
MP1	NIWs	65	23	58	40
	D1 ITs	15	21	40	54
	D2 ITs	10	11	56	39
MP2	NIWs	77	15	67	32
	D1 ITs	22	14	43	51
MP3	NIWs	55	28	54	44
	D1 ITs	18	19	37	58
	D2 ITs	8	9	47	50
MP4	NIWs	66	12	70	27
	D1 ITs	23	30	40	48
	D2 ITs	16	19	48	44
MP5	NIWs	80	10	75	24
	D1 ITs	26	25	47	48
	D2 ITs	13	16	44	46
MP6	NIWs	67	21	63	36
	D1 ITs	12	22	46	52
	D2 ITs	10	9	49	48

averaged currents cannot be regarded as the barotropic currents, but they have no contribution to the shear. Similar results are found from the zonal shear caused by the NIWs and ITs (Fig. 6). Table 2 lists the proportions of upgoing

and downgoing components in current variance and shear of NIWs, D1 and D2 ITs at the six moorings, from which the aforementioned analyses are quantified. In addition, the proportion of upgoing component (downward energy propagation) in the NIWs varies at the six moorings to some extent, suggesting the NIWs are also affected by local conditions.

3.3 Spatial pattern

Although the observation periods are various for the six moorings, all of them are longer than the typical periods of SICs, NIWs and ITs investigated in this study. Therefore, the observation-period-averaged shear in each frequency band at each mooring is calculated to show the spatial pattern of shear induced by SICs, NIWs and ITs in this area (Fig. 7). Note that shear does not satisfy the linear superposition and, therefore, the sum of shear caused by SICs, NIWs, D1 and D2 ITs may exceed the total shear. Overall, both the total shear and shear in different frequency bands exhibit a surface-intensified pattern and a decreasing trend with depth. However, the shear shows various intensities and structures at different moorings. The total shear at MP3 and MP6 is stronger than that at other moorings. At MP6, the strongest total shear (0.018 s^{-1}) appears at 60 m depth and decreases to 0.01 s^{-1} at 100 m depth below which the total shear almost keeps invariant. At MP3, the total shear has a 25% decrease within 300 m, from 0.012 s^{-1} at 150 m depth to 0.009 s^{-1} at 450 m depth. At the other four moorings (MP1, MP2, MP4 and MP5), the total shear is approximate $0.01\text{--}0.012 \text{ s}^{-1}$ at 100 m depth and $0.006\text{--}0.007 \text{ s}^{-1}$ at 400 m depth, corresponding to a 40–50% decrease within

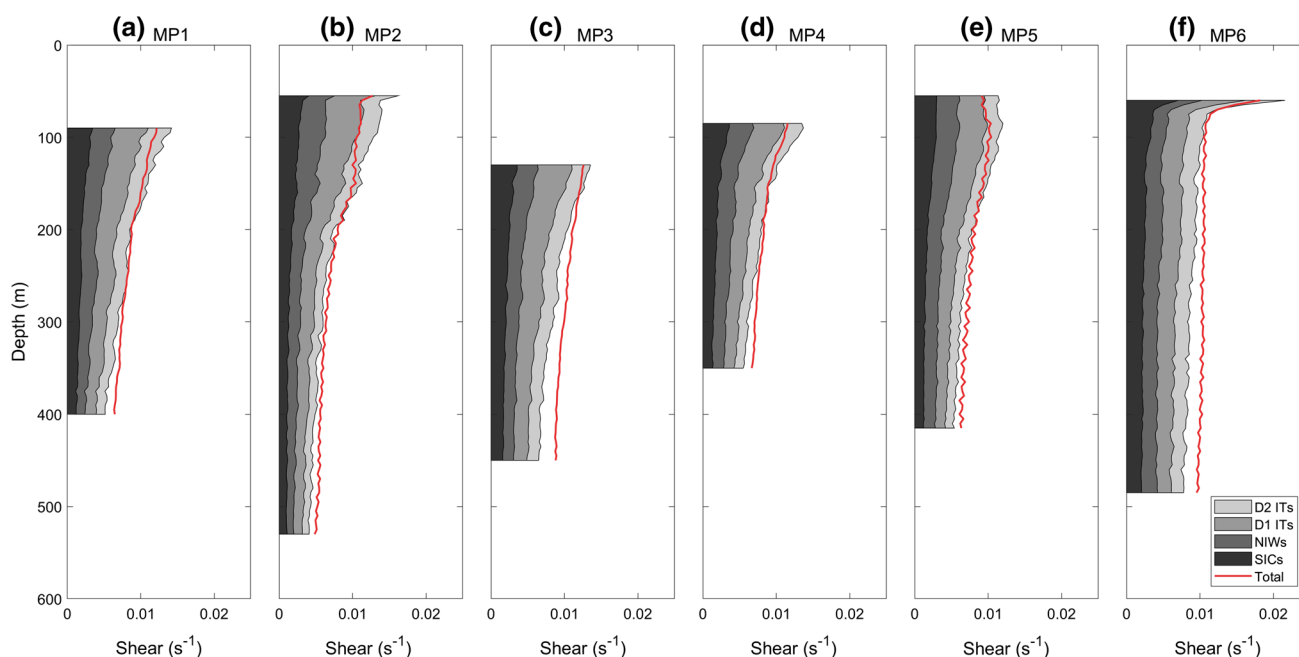


Fig. 7 Vertical structures of the total shear (red lines) and shear caused by motions in different frequency bands (stacked areas) at moorings **a–f** MP1–MP6 (color figure online)

Table 3 Time-depth averaged shear (unit: s^{-1}) caused by SICs, NIWs, D1 and D2 ITs as well as their proportions (in the brackets) in the total shear at the six moorings

Moorings	SICs	NIWs	D1 ITs	D2 ITs
MP1	0.0020 (23%)	0.0020 (24%)	0.0026 (30%)	0.0019 (22%)
MP2	0.0016 (22%)	0.0018 (25%)	0.0023 (32%)	0.0014 (20%)
MP3	0.0022 (21%)	0.0019 (19%)	0.0028 (28%)	0.0019 (19%)
MP4	0.0020 (24%)	0.0021 (26%)	0.0024 (30%)	0.0016 (20%)
MP5	0.0018 (23%)	0.0021 (27%)	0.0023 (30%)	0.0015 (19%)
MP6	0.0025 (24%)	0.0021 (20%)	0.0025 (24%)	0.0020 (19%)

300 meters. At each mooring, the shear caused by SICs, NIWs and ITs shares a similar pattern to the total shear.

Although shear does not satisfy the linear superposition, we still calculate proportions of the shear caused by SICs, NIWs and ITs in the total shear to evaluate their relative importance, which are listed in Table 3. At all the six moorings, the shear caused by D1 and D2 ITs is the strongest and weakest, respectively, consistent with the results of wavenumber frequency spectra shown in Fig. 4b. However, the intensity of shear caused by SICs and NIWs depends on locations: Near the LS (MP1, MP3 and MP6), the shear caused by SICs is stronger than or comparable to that caused by NIWs; whereas in the SCS Basin (MP2, MP4 and MP5), the NIWs lead to stronger shear than SICs.

As a comparison, we also calculate the current variance of SICs, NIWs, D1 and D2 ITs at the six moorings, of

which the vertical structures are shown in Fig. 8 and the proportions in the total variance are listed in Table 4. As shown in Fig. 8 and Table 4, the SICs and D1 ITs dominate the motions at all the six moorings, the sum of which accounts for more than 50% of the total variance. However, the intensities of SICs and D1 ITs vary significantly with moorings. Due to the influence of Kuroshio, SICs at MP6 are the strongest among all the moorings, whose current variance is 2–7 times larger than that of SICs at other moorings and 4.3 times larger than that of local D1 ITs. However, the SICs at MP2 are the weakest, whose variance is approximately half of that of local D1 ITs, although D1 ITs are comparable at MP2 and MP6. The D2 ITs are weaker than the SICs and D1 ITs, which account for 6–16% of the total variance at the six moorings. The NIWs are the weakest, whose time-depth averaged variance is 1–2 orders smaller than that of SICs and ITs. The NIWs only occupy 2–7% of the total variance, which is largely due to their intermittency. Combining the results of shear and current variance at the six moorings, we can obtain the following conclusions: (a) Although NIWs are the weakest in the time-depth averaged variance, they have a significant contribution to the upper ocean shear in the northern SCS, which is comparable to that caused by SICs and ITs. (b) In contrast to the NIWs, SICs are the strongest motion at some moorings, but they cannot cause the strongest shear. (c) The D1 and D2 ITs cause the strongest and weakest shear at all the six moorings, respectively.

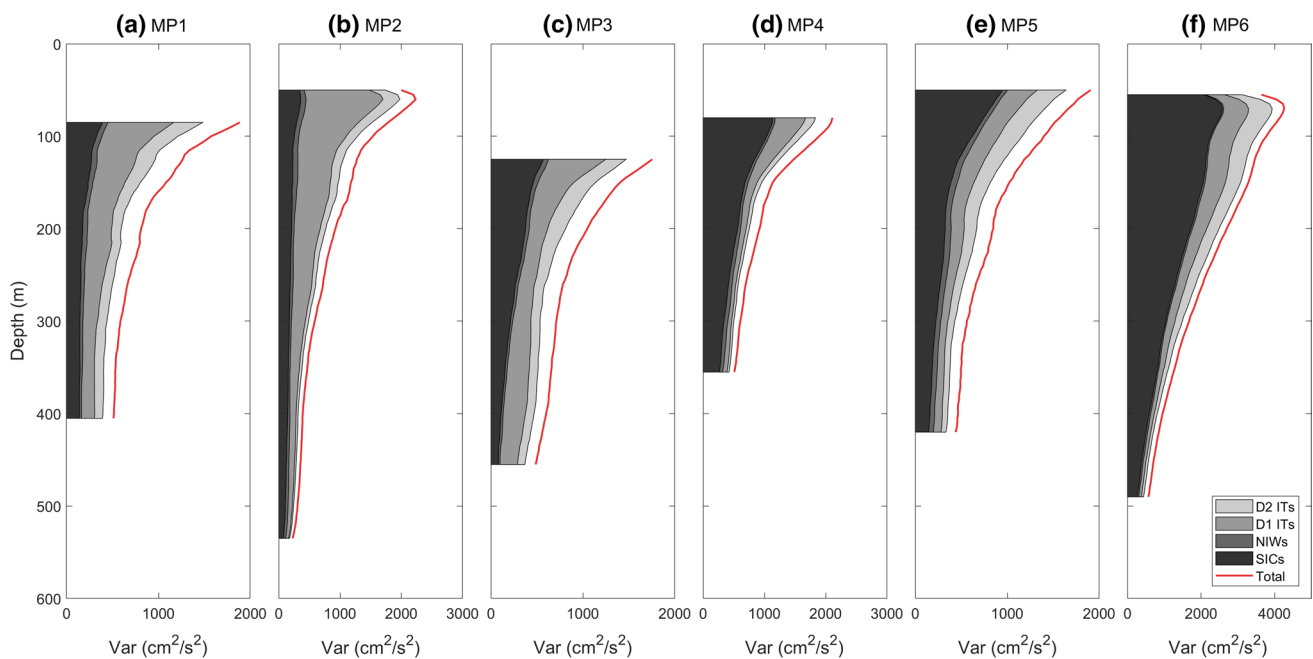


Fig. 8 Same as Fig. 7 but for current variance. Note that the horizontal axes vary with subfigures

Table 4 Same as Table 3 but for current variance (unit: cm^2/s^2)

Mooring	SICs	NIWs	D1 ITs	D2 ITs
MP1	188 (23%)	42 (5%)	260 (31%)	133 (16%)
MP2	184 (23%)	49 (6%)	343 (43%)	82 (10%)
MP3	255 (30%)	31 (4%)	245 (29%)	134 (16%)
MP4	570 (58%)	52 (5%)	142 (14%)	64 (6%)
MP5	355 (41%)	57 (7%)	141 (16%)	136 (16%)
MP6	1301 (62%)	41 (2%)	305 (14%)	267 (13%)

3.4 Temporal variation

To examine the temporal variation of shear, Fig. 9 displays the depth-averaged shear caused by SICs, NIWs, D1 and D2 ITs at MP3, MP5 and MP6. At MP3, D1 ITs cause the strongest shear almost over the entire observation period and are followed by SICs. The shear caused by NIWs and D2 ITs is comparable and a little weaker than that caused by SICs. At MP5, the shear caused by D1 ITs is significantly enhanced in November and December 2010, and the shear caused by NIWs is enhanced during the five NIW events (Cao et al. 2018). At other time, the shear caused by SICs, NIWs and D1 ITs is comparable and apparently stronger than that caused by D2 ITs. At MP6, the shear caused by SICs and D1 ITs has a similar trend and is a little stronger than that caused by NIWs and D2 ITs. The shear caused by NIWs and D2 ITs is comparable during the observation period except in late October when typhoon Chaba generated intense NIWs with strong shear. In addition, the shear

caused by SICs and NIWs exhibits apparent intermittence, which is consistent with their dynamical variability.

Although both D1 and D2 ITs at the six moorings are dominated by the coherent component which exhibits apparent spring-neap cycles of approximately 14 days (Cao et al. 2017), we still find significant high-frequency-signals on the shear of D1 and D2 ITs (Fig. 9). Therefore, we calculate the shear caused by the coherent and incoherent components of D1 and D2 ITs at the six moorings. Figures 10 and 11 illustrate the results at MP3 and MP5, respectively. As a comparison, the current variance of coherent and incoherent components of D1 and D2 ITs is also shown in Figs. 10 and 11. At the two moorings, the shear caused by the coherent components of D1 and D2 ITs exhibits apparent spring-neap cycles, which is consistent with the variation of their current variance. However, the shear caused by the incoherent components of D1 and D2 ITs does not exhibit regular temporal variations. Indeed, power spectra (not shown) of shear caused by the incoherent components exhibit many peaks in a broad frequency range from 0.03 to 0.3 cpd (corresponding to periods of 3.3 to 33.3 days). Whereas power spectra of shear caused by the coherent components are dominated by the spring-neap cycles. Indeed, the shear caused by the incoherent components is 2–4 times larger than that caused by the coherent components for both D1 and D2 ITs at the six moorings, which is the cause of high-frequency signals on the shear of D1 and D2 ITs (Fig. 9). Given that both D1 and D2 ITs at the six moorings are dominated by the coherent component, this result also suggests that the incoherent component has a larger vertical wavenumber than the coherent

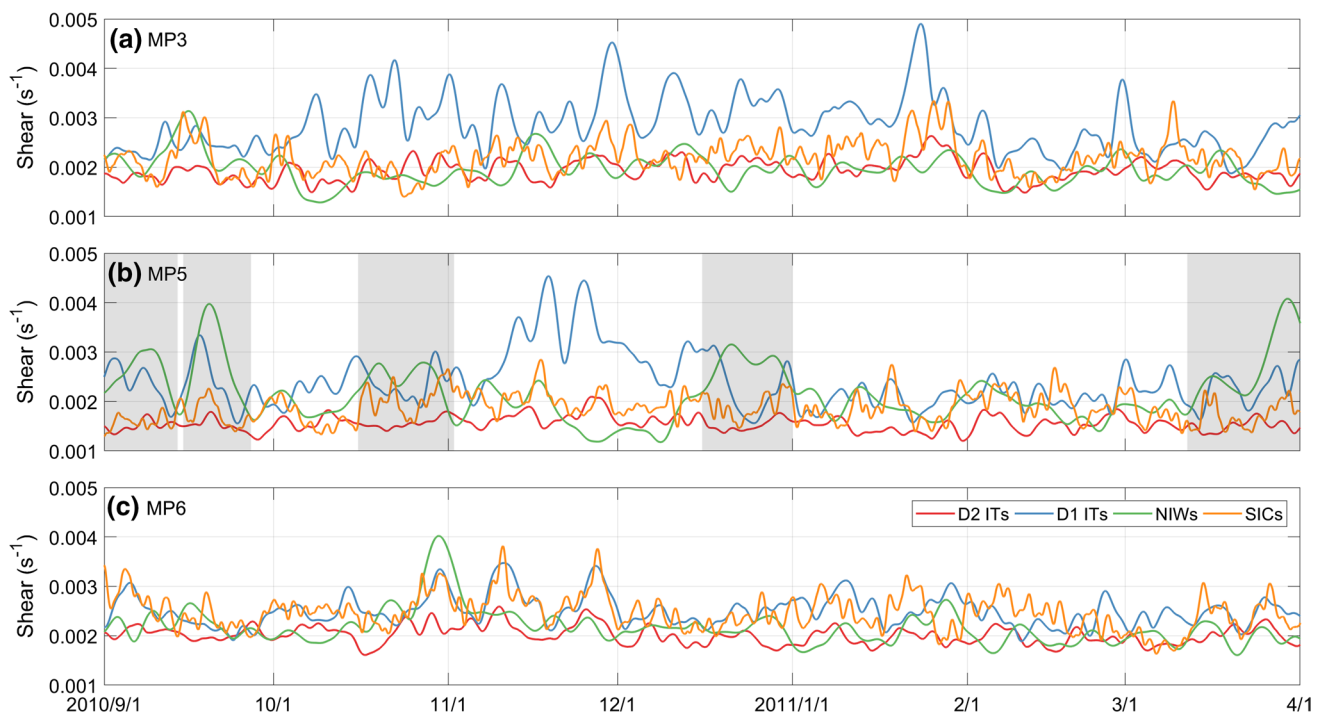


Fig. 9 Depth averaged shear caused by SICs (yellow), NIWs (green), D1 (blue) and D2 (red) ITs at **a** MP3, **b** MP5 and **c** MP6. Note that the shear caused by NIWs, D1 and D2 ITs has been lowpass filtered

to remove oscillations in their own frequencies. Shadings in subfigure **b** indicate the five NIW events at MP5 (color figure online)

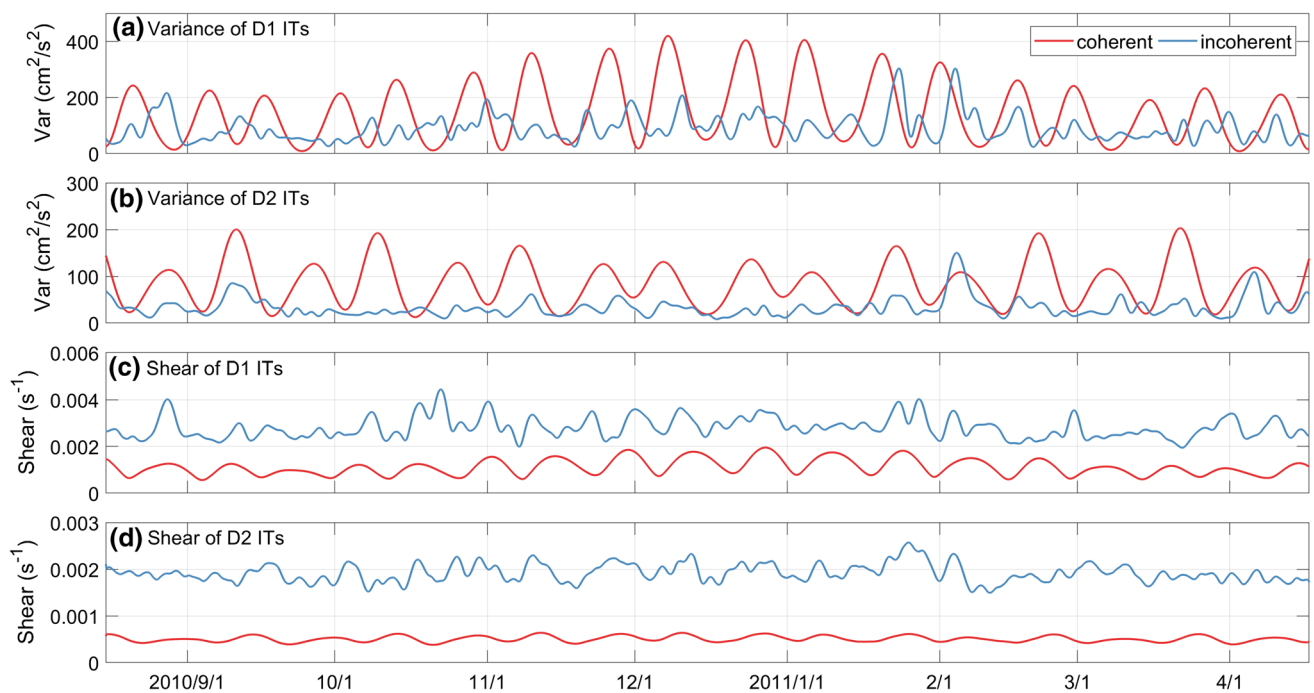


Fig. 10 Depth averaged **a, b** current variance and **c, d** shear of the coherent (red) and incoherent (blue) components of **a, c** D1 and **b, d** D2 ITs at MP3. Note that both the current variance and shear have

been lowpass filtered to remove oscillations in their own frequencies (color figure online)

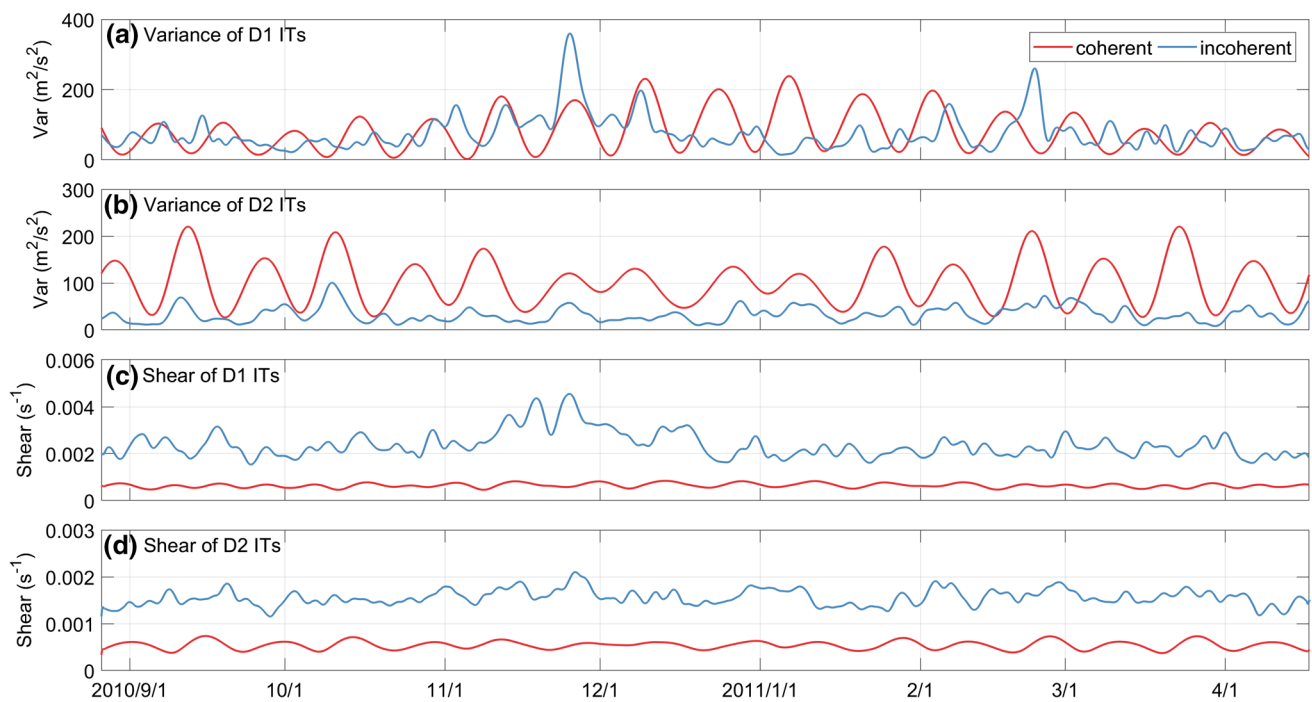


Fig. 11 Same as Fig. 10 but for MP5

component, which generally agrees with the conclusion of Liu et al. (2016). In addition, the enhanced shear of the D1 ITs at MP5 in November and December 2010 (Fig. 9b) is actually induced by the incoherent components, which is clearly shown in Fig. 11.

3.5 Shear induced by the ME pair

Because a ME pair (a CE and an AE) passed through the mooring area from late October to early December 2010 (Fig. 2), its contribution to the upper ocean shear is studied in this section. Figure 12 illustrates the time-depth maps of SICs as well as corresponding current variance and shear at MP4 and MP5. Combining with the sea level anomaly and surface geostrophic current data (Fig. 2), we find that both MP4 and MP5 captured the signal of the ME pair: At MP4, the CE was first detected on 22 October and lasted to 2 November, then the AE arrived and lasted to 2 December. At MP5, the CE was observed from 23 October to 6 November and the AE from 6 November to 2 December. Because both MP4 and MP5 located at the northern edge of the ME pair (Fig. 2), the meridional SICs are almost northward in the CE and AE periods, whereas the zonal SICs apparently change directions. The current variance is significantly enhanced during the CE and AE periods (Fig. 12c, g). However, the corresponding shear does not show remarkable enhancement during the CE and AE periods, especially below 150 m depth (Fig. 12d, h).

Figure 13 illustrates the current variance and shear of SICs averaged in both the CE and AE periods at the two moorings. As a comparison, those averaged in the whole observation periods are also shown. We find that the relation between current variance (intensity) of MEs and their contributions to shear is complicated. On one hand, the current variance of the AE at MP4 is approximate 1.5 times larger than that averaged in the whole period, whereas the shear induced by the AE is almost the same as the whole-period-averaged value. On the other hand, the CE is apparently stronger than the AE at MP5, while their contributions to shear are comparable. Moreover, the shear caused by MEs below 150 depth at the two moorings is comparable to the whole-period-averaged value and varies slightly with changes of MEs. These results suggest that the MEs do not significantly enhance the ocean shear, especially below 150 m depth. In addition, these results are generally consistent with the observation of Liu et al. (2017) who revealed that the turbulent kinetic energy dissipation rate and diapycnal diffusivity at the north flank of the Mindanao Eddy were lower due to the smaller shear and larger Richardson number ($Ri = N^2/s^2$ and N is the local buoyancy frequency).

4 Discussion

At the six moorings, NIWs only account for 2–7% of the total current variance, but the shear caused by NIWs is approximate one fifth to one quarter of the total shear. In

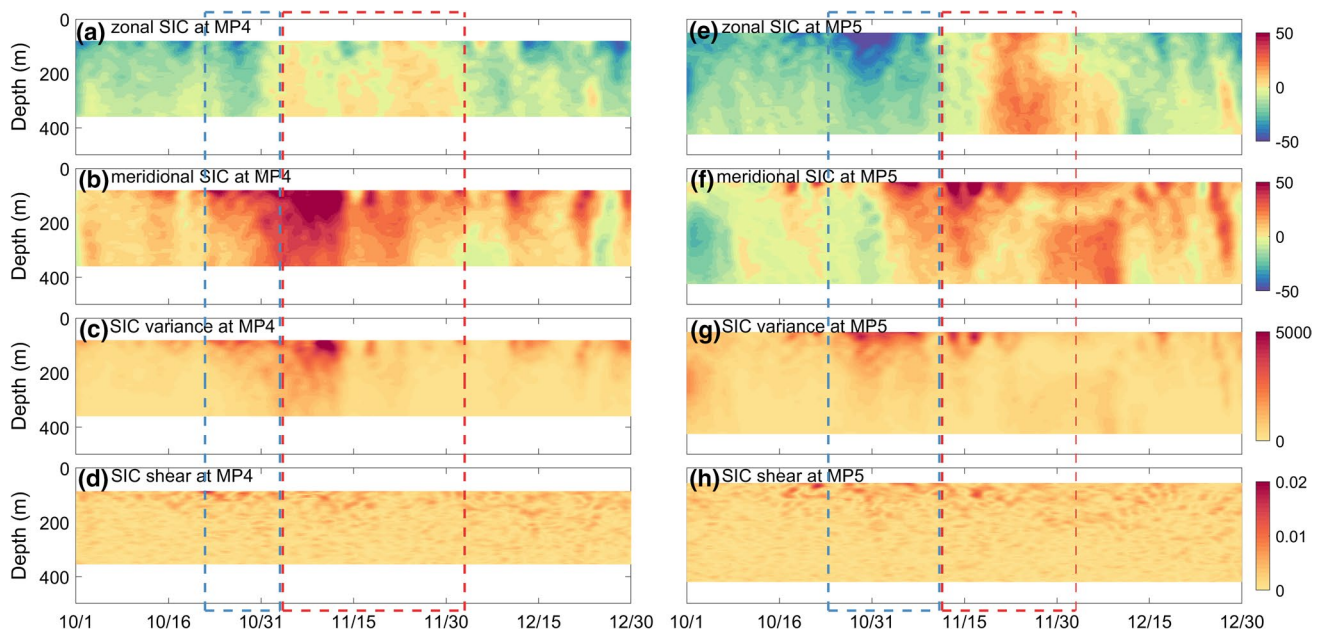


Fig. 12 **a, e** Zonal and **b, f** meridional components (unit: cm/s), **c, g** current variance (unit: cm^2/s^2) and **d, h** shear (unit: s^{-1}) of SICs at **a–d** MP4 and **e–h** MP5. The blue and red dashed boxes indicate the CE and AE periods, respectively

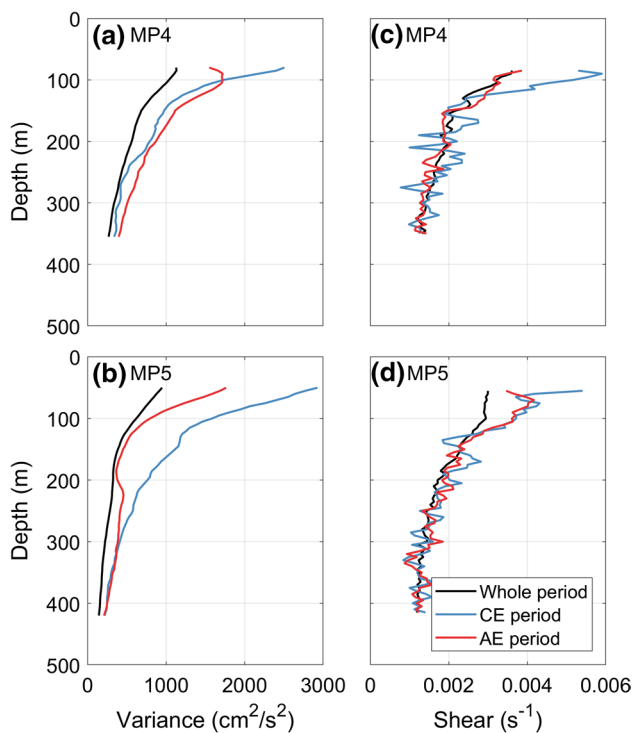


Fig. 13 Vertical structures of **a, b** current variance and **c, d** shear of SICs averaged during the whole observation period (black), the CE (blue) and AE (red) periods at **a, c** MP4 and **b, d** MP5 (color figure online)

contrast, the D1 and D2 ITs account for 14–43% and 6–16% of the total current variance and contribute to 24–32% and 6–16% of the total shear, respectively. Assuming that NIWs

and ITs have comparable horizontal scales in this area, this result can be preliminarily explained. According to the theory of internal waves (Pedlosky 2003), the vertical and horizontal wavenumbers (m and k) of internal waves satisfy the following equation:

$$\omega^2 = f^2 + (N^2 - f^2) \frac{k^2}{k^2 + m^2} \approx f^2 + N^2 \frac{k^2}{k^2 + m^2}, \quad (4)$$

where ω is the intrinsic frequency of internal waves, N and f are the buoyancy and local inertial frequencies and satisfy the relation $f < N$. Because NIWs and ITs have comparable horizontal scales (k), the smaller intrinsic frequency of NIWs would lead to larger vertical wavenumber m (corresponding to smaller vertical wavelength) than the ITs. Result shown in Fig. 4a confirms that the NIWs here indeed have larger vertical wavenumber than the D1 and D2 ITs. Therefore, the weaker NIWs can cause stronger shear, when compared with ITs. This result indicates that we need to pay more attention to the generation, propagation and dissipation of high-wavenumber NIWs when developing local parameterization of turbulent mixing.

Previous observations have shown the enhanced mixing in the northern SCS, which is thought to be attributed to ITs radiated from the LS (Tian et al. 2009; Yang et al. 2016). In this study, we find that the D1 ITs cause stronger shear than the D2 ITs at all the six moorings (Table 3). Given that shear instability drives the most turbulence in the ocean (Alford et al. 2017), this result implies that the D1 ITs should account more for the enhanced mixing in the northern SCS than the D2 ITs, at least in the upper ocean. It could be largely attributed to the

different reflection patterns of D1 and D2 ITs at the continental slope of the northern SCS. The continental slope is supercritical for D1 ITs so that the incoming D1 IT are reflected back and trapped in the SCS Basin (Klymak et al. 2011; Wu et al. 2013; Guo et al. 2018). In contrast, the continental slope is subcritical for D2 ITs. As a result, the incoming D2 ITs can directly transmit onto the continental slope. This difference makes the D1 current variance larger than the D2 in the SCS Basin. Moreover, the reflected D1 ITs would have a different propagating direction from the incoming ones, whereas this phenomenon is absent for D2 ITs. Thus, the D1 ITs have larger vertical wavenumber than D2 ITs in the SCS Basin and contribute more to the shear. In addition, it is also the cause for the difference between shear in the SCS Basin and that on the continental shelf and slope of the northern SCS (Xu et al. 2011, 2013). Because most D1 ITs are trapped in the SCS Basin due to the reflection, the shear caused by D2 ITs is comparable to or stronger than that caused by D1 ITs on the continental shelf and slope of the northern SCS (Xu et al. 2011, 2013). Also note that the westward D1 energy flux radiated from the LS into the SCS is smaller than that of the D2 ITs (Zhao 2014; Alford et al. 2015), but the D1 ITs cause stronger shear than the D2 ITs in the SCS Basin due to reflection. In other words, it is the reflection rather than the generation at the LS leads to the enhancement of current variance and shear of the D1 ITs in the SCS Basin. All these results imply that we need to consider the different contributions of D1 and D2 ITs at different areas when developing parameterization of turbulent mixing in the SCS.

Although both D1 and D2 ITs in the northern SCS are dominated by the coherent component, the shear induced by the incoherent component is stronger than that induced by the coherent component. In other words, the incoherent component of ITs has a considerable impact on the ocean shear and hence turbulent mixing. Therefore, the generation and dissipation of incoherent ITs should be taken into consideration for the development of local parameterization of turbulent mixing. Furthermore, although the direct contribution of MEs to upper ocean shear is limited, they can indeed change the local stratification and contribute to the generation of incoherent ITs (Eich et al. 2004; van Haren 2004; van Aken et al. 2007; Kerry et al. 2016). Hence, the influence of MEs on incoherent ITs cannot be neglected in the parameterization.

5 Conclusions

Based on moored current observations from the SCS Internal Wave Experiment (2010–2011), this study shows the shear in the upper ocean of the northern SCS. Wavenumber frequency spectra of current and shear show that SICs, NIWs, D1 and D2 ITs are the dominant motions in this area. By calculating current variance and shear caused by these

motions, this study shows the great contribution of NIWs to upper ocean shear. Although NIWs only account for 2–7% of the total current variance, the shear caused by NIWs is approximate one fifth to one-quarter of the total shear. In contrast, the D1 and D2 ITs account for 14–43% and 6–16% of the total current variance and contribute to 24–32% and 6–16% of the total shear, respectively. Although the westward D1 IT energy flux radiated from the LS into the SCS is a little smaller than that of the D2, the D1 ITs indeed cause greater current variance and stronger shear in the SCS Basin than the D2, which is largely due to their different reflection patterns at the continental slope of the northern SCS. Moreover, for both D1 and D2 ITs at the moorings, the coherent component dominates the current variance, whereas the incoherent component contributes more to the shear, suggesting that the incoherent component has larger vertical wavenumber than the coherent component. Indeed, the shear caused by the incoherent component is 2–4 times larger than that caused by the coherent component for both D1 and D2 ITs. A case study shows that the mesoscale eddy pair occurring between 22 October and 2 December 2010 does not significantly enhance the upper ocean shear at two moorings especially below 150 m depth, although it contributes a lot to the current variance. Given that shear instability drives the most turbulence in the ocean (Alford et al. 2017), we hope that these results can provide insight into the development of local parameterization of turbulent mixing.

Acknowledgements This study is supported by the National Key Research and Development Program of China through Grants 2017YFA0604102, 2016YFC1401404 and 2016YFC1402304, and the National Natural Science Foundation of China through Grants 41806012 and 41876015. The authors deeply thank Physical Oceanography Laboratory as well as Professor Wei Zhao for providing the mooring observations. The authors also thank the Editor and two anonymous Reviewers for their insightful comments and valuable suggestions.

References

- Alford MH, Mackinnon JA, Nash JD et al (2011) Energy flux and dissipation in Luzon Strait: two tales of two ridges. *J Phys Oceanogr* 41:2211–2222
- Alford MH, Peacock T, Mackinnon JA et al (2015) Corrigendum: the formation and fate of internal waves in the South China Sea. *Nature* 521:65–69
- Alford MH, Mackinnon JA, Pinkel R, Klymak JD (2017) Space-time scales of shear in the North Pacific. *J Phys Oceanogr* 47:2455–2478
- Buijsman MC, Klymak JM, Legg S et al (2014) Three-dimensional double-ridge internal tide resonance in Luzon Strait. *J Phys Oceanogr* 44:850–869
- Cao A-Z, Li B-T, Lv X-Q (2015) Extraction of internal tidal currents and reconstruction of full-depth tidal currents from mooring observations. *J Atmos Ocean Technol* 32:1414–1424

- Cao A, Guo Z, Lv X, Song J, Zhang J (2017) Coherent and incoherent features, seasonal behaviors and spatial variations of internal tides in the northern South China Sea. *J Mar Syst* 172:75–83
- Cao A, Guo Z, Song J, Lv X, He H, Fan W (2018) Near-inertial waves and their underlying mechanisms based on the South China Sea Internal Wave Experiment (2010–2011). *J Geophys Res Oceans* 123:5026–5040
- Chen G, Hou Y, Chu X, Qi P (2009) The variability of eddy kinetic energy in the South China Sea deduced from satellite altimeter data. *Chin J Oceanol Limnol* 27:943–954
- Chen G, Hou Y, Chu X (2011) Mesoscale eddies in the South China Sea: mean properties, spatiotemporal variability, and impact on thermohaline structure. *J Geophys Res*. <https://doi.org/10.1029/2010jc006716>
- Chen G, Xue H, Wang D, Xie Q (2013) Observed near-inertial kinetic energy in the northwestern South China Sea. *J Geophys Res Oceans* 118:4965–4977. <https://doi.org/10.1002/jgrc.20371>
- Cheng X, Qi Y (2010) Variations of eddy kinetic energy in the South China Sea. *J Oceanogr* 66:85–94
- Eich ML, Merrifield MA, Alford MH (2004) Structure and variability of semidiurnal internal tides in Mamala Bay, Hawaii. *J Geophys Res*. <https://doi.org/10.1029/2003jc002049>
- Fox-Kemper B, Adcroft A, Böning CW et al (2019) Challenges and prospects in ocean circulation models. *Front Mar Sci* 6:65. <https://doi.org/10.3389/fmars.2019.00065>
- Guan S, Zhao W, Huthnance J, Tian J, Wang J (2014) Observed upper ocean response to typhoon Megi (2010) in the Northern South China Sea. *J Geophys Res Oceans* 119:3134–3157
- Guo P, Fang W, Liu C, Qiu F (2012) Seasonal characteristics of internal tides on the continental shelf in the northern South China Sea. *J Geophys Res*. <https://doi.org/10.1029/2011jc007215>
- Guo Z, Cao A, Lv X (2018) Seasonal variation and modal content of internal tides in the northern South China Sea. *Chin J Oceanol Limnol*. <https://doi.org/10.1007/s00343-018-6352-1>
- Hibiya T, Nagasawa M (2004) Latitudinal dependence of diapycnal diffusivity in the thermocline estimated using a finescale parameterization. *Geophys Res Lett* 31:L01301
- Hibiya T, Niwa Y, Nakajima K, Sugihara N (1996) Direct numerical simulation of the roll-off range of internal wave shear spectra in the ocean. *J Geophys Res* 101:14123–14129
- Hibiya T, Niwa Y, Fujiwara K (1998) Numerical experiments of nonlinear energy transfer within the oceanic internal wave spectrum. *J Geophys Res* 103:18715–18722
- Hibiya T, Nagasawa M, Niwa Y (2002) Nonlinear energy transfer within the oceanic internal wave spectrum at mid and high latitudes. *J Geophys Res* 107:3207
- Kerry CG, Powell BS, Carter GS (2016) Quantifying the Incoherent M2 Internal Tide in the Philippine Sea. *J Phys Oceanogr* 46:2483–2491
- Klymak JM, Alford MH, Pinkel R et al (2011) The breaking and scattering of the internal tide on a continental slope. *J Phys Oceanogr* 41:926–945
- Leaman KD, Sanford TB (1975) Vertical energy propagation of inertial waves: a vector spectral analysis of velocity profiles. *J Geophys Res* 80:1975–1978
- Lee I-H, Wang Y-H, Yang Y, Wang D-P (2012) Temporal variability of internal tides in the northeast South China Sea. *J Geophys Res*. <https://doi.org/10.1029/2011jc007518>
- Li B, Cao A, Lv X (2015a) Three-dimensional numerical simulation of M2 internal tides in the Luzon Strait. *Acta Oceanol Sin* 34:55–62
- Li J, Liu J, Cai S, Pan J (2015b) The spatiotemporal variation of the wind-induced near-inertial energy flux in the mixed layer of the South China Sea. *Acta Oceanol Sin* 34:66–72
- Li Q, Wang B, Chen X, Chen X, Park J-H (2016) Variability of nonlinear internal waves in the South China Sea affected by the Kuroshio and mesoscale eddies. *J Geophys Res Oceans* 121:2098–2118
- Liu Q, Xie X, Shang X, Chen G (2016) Coherent and incoherent internal tides in the southern South China Sea. *Chin J Oceanol Limnol* 34:1–9
- Liu Z, Lian Q, Zhang F et al (2017) Weak thermocline mixing in the North Pacific low-latitude western boundary current system. *Geophys Res Lett* 44:10530–10539
- Ma BB, Lien R-C, Ko DS (2013) The variability of internal tides in the Northern South China Sea. *J Oceanogr* 69:619–630
- MacKinnon JA, Alford MH, Sun O, Pinkel R, Zhao Z, Klymak J (2013) Parametric subharmonic instability of the internal tide at 29°N. *J Phys Oceanogr* 43:17–28
- MacKinnon JA, Zhao Z, Whalen CB et al (2017) Climate process team on internal wave-driven ocean mixing. *Bull Am Meteorol Soc* 98:2429–2454
- Nagasawa M, Niwa Y, Hibiya T (2000) Spatial and temporal distribution of the wind-induced internal wave energy available for deep water mixing in the North Pacific. *J Geophys Res* 105:13933–13943
- Nagasawa M, Hibiya T, Ruruichi N, Takagi S (2005) Temporal variability of high vertical wavenumber shear over the Izu-Ogasawara ridge. *J Oceanogr* 61:1101–1105
- Nash JD, Shroyer EL, Kelly SM, Inall ME, Duda TF, Levine MD, Jones NL, Musgrave RC (2012) Are any coastal internal tides predictable? *Oceanography* 25:80–95
- Pawlowicz R, Beardsley B, Lentz S (2002) Classical tidal harmonic analysis including error estimates in MATLAB using T_TIDE. *Comput Geosci* 28:929–937
- Pedlosky J (2003) *Waves in the ocean and atmosphere*. Springer, Berlin
- Pickering A, Alford M, Nash J et al (2015) Structure and variability of internal tides in Luzon Strait. *J Phys Oceanogr* 45:1574–1594
- Shang X, Liu Q, Xie X, Chen G, Chen R (2015) Characteristics and seasonal variability of internal tides in the southern South China Sea. *Deep Sea Res Part I* 98:43–52
- Simmons HL, Hallberg RW, Arbic BK (2004) Internal wave generation in a global baroclinic tide model. *Deep-Sea Res Part II* 51:3043–3068
- Sun Z, Hu J, Zheng Q, Li C (2011) Strong near-inertial oscillations in geostrophic shear in the northern South China Sea. *J Oceanogr* 67:377–384
- Sun Z, Zhang Z, Zhao W, Tian J (2016) Interannual modulation of eddy kinetic energy in the northeastern South China Sea as revealed by an eddy-resolving OGCM. *J Geophys Res Oceans* 121:3190–3201
- Tian J, Yang Q, Zhao W (2009) Enhanced diapycnal mixing in the South China Sea. *J Phys Oceanogr* 39:3191–3203
- van Aken HM, van Haren H, Maas LRM (2007) The high-resolution vertical structure of internal tides and near-inertial waves measured with an ADCP over the continental slope in the Bay of Biscay. *Deep Sea Res Part I* 54:533–556
- van Haren H (2004) Incoherent internal tidal currents in the deep ocean. *Ocean Dyn* 54:66–76
- Wang G, Su J, Chu PC (2003) Mesoscale eddies in the South China Sea observed with altimeter data. *Geophys Res Lett*. <https://doi.org/10.1029/2003gl018532>
- Wang G, Su J, Ding Y, Chen D (2007) Tropical cyclone genesis over the South China Sea. *J Mar Syst* 68:318–326
- Wu L, Miao C, Zhao W (2013) Patterns of K1 and M2 internal tides and their seasonal variations in the northern South China Sea. *J Oceanogr* 69:481–494
- Xie XH, Shang XD, van Haren H, Chen GY, Zhang YZ (2011) Observations of parametric subharmonic instability-induced near-inertial waves equatorward of the critical diurnal latitude. *Geophys Res Lett* 38:15. <https://doi.org/10.1029/2010gl046521>

- Xu Z, Yin B, Hou Y (2011) Multimodal structure of the internal tides on the continental shelf of the northwestern South China Sea. *Estuar Coast Shelf Sci* 95:178–185
- Xu Z, Yin B, Hou Y, Xu Y (2013) Variability of internal tides and near-inertial waves on the continental slope of the northwestern South China Sea. *J Geophys Res* 118:197–211
- Xu Z, Yin B, Hou Y, Liu AK (2014) Seasonal variability and north-south asymmetry of internal tides in the deep basin west of the Luzon Strait. *J Mar Syst* 134:101–112
- Xu Z, Liu K, Yin B, Zhao Z, Wang Y, Li Q (2016) Long-range propagation and associated variability of internal tides in the South China Sea. *J Geophys Res* 121:8268–8286
- Yang B, Hou Y (2014) Near-inertial waves in the wake of 2011 Typhoon Nesat in the northern South China Sea. *Acta Oceanol Sin* 33:102–111
- Yang B, Hou Y, Hu P, Liu Z, Liu Y (2015) Shallow ocean response to tropical cyclones observed on the continental shelf of the northwestern South China Sea. *J Geophys Res Oceans* 120:3817–3836
- Yang Q, Zhao W, Liang X, Tian J (2016) Three-dimensional distribution of turbulent mixing in the South China Sea. *J Phys Oceanogr* 46:769–788
- Yang Q, Zhao W, Liang X, Dong J, Tian J (2017) Elevated mixing in the periphery of mesoscale eddies in the South China Sea. *J Phys Oceanogr* 47:895–907
- Zhang Z, Zhao W, Tian J, Liang X (2013) A mesoscale eddy pair southwest of Taiwan and its influence on deep circulation. *J Geophys Res Oceans* 118:6479–6494
- Zhang Z, Wang W, Qiu B (2014) Oceanic mass transport by mesoscale eddies. *Science*. <https://doi.org/10.1126/science.1252418>
- Zhang H, Chen D, Zhou L, Liu X, Ding T, Zhou B (2016a) Upper ocean response to typhoon Kalmaegi (2014). *J Geophys Res Oceans* 121:6520–6535
- Zhang Z, Tian J, Qiu B et al (2016b) Observed 3D Structure, Generation, and Dissipation of Oceanic Mesoscale Eddies in the South China Sea. *Sci Rep*. <https://doi.org/10.1038/srep24349>
- Zhao Z (2014) Internal tide radiation from the Luzon Strait. *J Geophys Res Oceans* 119:5434–5448
- Zhao Z, Alford MH, Mackinnon JA, Pinkel R (2010) Long-range propagation of the semidiurnal internal tide from the Hawaiian Ridge. *J Phys Oceanogr* 40:713–736